ACS APPLIED MATERIALS & INTERFACES

Research Article

www.acsami.org

Bioinspired in Situ Growth of Conversion Films with Underwater Superoleophobicity and Excellent Self-Cleaning Performance

Zhiwei Wang, Liqun Zhu, Weiping Li, and Huicong Liu*

Key Laboratory of Aerospace Materials and Performance (Ministry of Education), School of Materials Science and Engineering, Beihang University, Beijing 100191, China

Supporting Information

ABSTRACT: Wax deposition during the production and transportation of crude oil is a global problem in oil industries. Fabrication of underwater self-cleaning materials can provide a new strategy to prohibit wax deposition. In this paper, conversion films on carbon steel with hierarchical micro/nanostructure are fabricated through a novel in situ alternating-current deposition method. The flower-like conversion films are composed of amorphous iron phosphate and present superhydrophilicity in air and superoleophobicity underwater. The conversion films can efficiently prevent the deposition of wax in water-contained crude oil, showing excellent self-cleaning performance. This facile and low-cost fabrication of a self-cleaning film provides a good strategy for underwater–oil prevention.

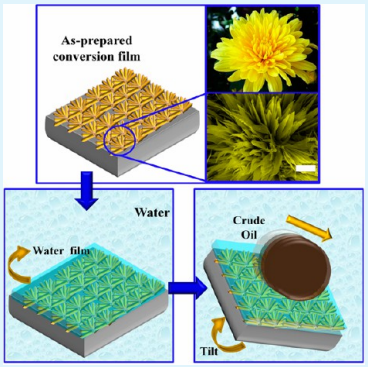

KEYWORDS: *conversion films, alternating current, self-cleaning, superoleophobic, crude oil, wax deposition*

1. INTRODUCTION

Wax deposition is a detrimental problem that happens during oil production and transportation when the temperature decreases.[1] Wax deposited in the transportation tube reduces the effective cross area and raises the flow resistance, which leads to great economic loss.[2] Many methods have been investigated to solve this problem.[3−6] However, all of these methods are either inefficient or costly. It is necessary and urgent to develop effective self-cleaning surfaces for wax prevention, especially in a facile and low-cost way.

The self-cleaning phenomenon is a special characteristic by which material keeps itself free of dirt and grime.[7−10] Fabricating superhydrophobic[11,12] or superoleophobic[13,14] functional materials with a low sliding angle (SA) is the most common way to create self-cleaning films. The surrounding has a great influence on the self-cleaning performance. As indicated in Cassie's theory,[15] air can be trapped in a water–solid interface when the water droplet is on a rough solid surface with low surface energy in an air environment. It provides an air–water–solid interface that reduces the contact area between water and solid, leading to high contact angle (CA) and low SA. Because water usually mixes in crude oil during oil production or transportation,[16] the water–oil–solid interface needs to be considered in the design of a self-cleaning film for application in crude oil. Similar to the role of air, water absorbed on a solid surface can improve the oleophobicity in a water–oil–solid interface,[17−20] which may provide the possibility for fabricating a self-cleaning film to prevent wax in water-contained crude oil. Nosonovsky et al.[21,22] studied the wetting transitions when solid surfaces were immersed in water and in contact with oil. Jiang and co-workers[23,24] have developed superhydrophilic and underwater superoleophobic materials-coated meshes for oil–water separation. Also, it was revealed that the underwater superoleophobicity of a clam's shell originated from the high-energy inorganic composition and surface hierarchical micro/nanostructure.[25,26] However, to the best of our knowledge, these underwater superoleophobic materials have rarely been used for wax prevention in crude oil. Besides, the previously reported fabrication process of the underwater superoleophobic materials is usually complicated and time-consuming (vary from a dozen of hours[25] to several days[24]).

Herein, inspired by the self-cleaning performance of the fish scale,[19] shark skin,[27] and clam's shell,[25] we constructed amorphous iron phosphate conversion films on carbon steel using a novel in situ alternating-current (ac) deposition method. The conversion films have flower-like structure and show superoleophobicity underwater with low oil adhesion, as shown in Figure 1. In water-contained crude oil, the conversion films prevent wax deposition and show excellent self-cleaning performance. Furthermore, this one-step fabrication process is simple and facile and only takes less than 4 h without further modification.

2. EXPERIMENTAL SECTION

2.1. Materials. Acetone, ethanol, and phosphoric acid were of analytical grade and were used for experiments reported in the present work. Carbon steel plates (40 mm × 20 mm × 2 mm) were

Received: July 29, 2013
Accepted: September 30, 2013
Published: September 30, 2013

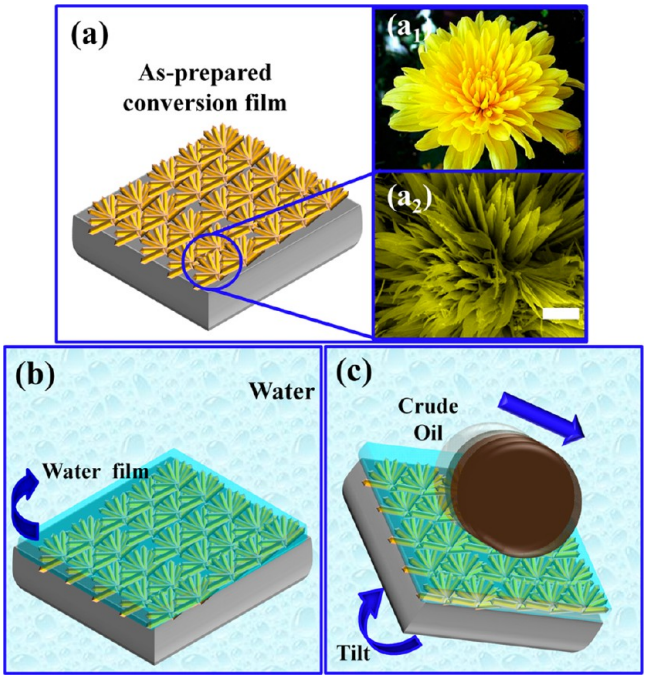

Figure 1. (a) Schematic illustration of the design of a conversion film. (a_1) Photograph of a real chrysanthemum (downloaded from the Internet: http://www.yuanlin8.com/plants/5684.html). (a_2) SEM image of the conversion film. The scale bar is 4 μm. (b and c) Underwater superoleophobic mechanism.

ultrasonically cleaned in acetone and then rinsed with deionized water sequentially before use.

2.2. ac Deposition. The carbon steel plates used as the electrodes were polished by sandpaper and cleaned by ethanol and deionized water sequentially. Then two pretreated carbon steel plates were immersed in a phosphoric acid aqueous solution under an ac voltage of 20 V and 50 Hz (see Supporting Information Figure S1). After ac deposition, carbon steel plates were taken out and rinsed by deionized water and ethanol.

2.3. Wax Deposition Test. The crude oil for wax deposition test was from Daqing Oilfield (in Hei Longjiang province, China), and the main characteristics are shown in Supporting Information Table S1. The wax deposition procedure was simulated in the laboratory using a self-designed apparatus based on the coldfinger method.[28] In the wax deposition test, crude oil was heated to 80 °C in a water bath and stirred thoroughly (ω = 20 rad·S^{-1}) to ensure complete dissolution and well-distribution of wax. Then the specimens were fixed onto the inner wall of the container. After the oil was kept at 80 °C for 0.5 h, it was cooled by circulating water cooling (water temperature is 30 °C). When the oil temperature decreased to 30 °C uniformly, the specimens were taken out and washed with water (30 °C) to erase the adherent oil. Macrographs of the specimens before and after the test were obtained by a digital camera (Olympus, E-PL1). For the clear color contrast between the deposition and clean areas, the quantitative determination of the wax deposition reduction rate (DR) was calculated according to eq 1:

$$\mathrm{DR}\ (\%) = \left(1 - \frac{S_d}{S_0}\right) \times 100\% \quad (1)$$

where S_d and S_0 are the deposition and total areas of the specimen, respectively.

2.4. CA Test. The CAs were measured using a contact angle meter (DSA 20, Krüss Instruments GmbH) on five different positions for each surface. The volume of an individual droplet in all measurements was about 6−10 μL. In the water CA (wCA) test, the samples were placed on the sample table. In the underwater−oil CA (oCA) test, the samples were upside down in a water-filled glass container because the density of oil was lower than water. First, samples were immersed in hot water ($T \approx 80$ °C to keep crude oil at the liquid state), and then a crude oil droplet was gently injected by a microsyringe on the surfaces.

2.5. Characterizations. Field-emission scanning electron microscopy (Camscan Apollo 300) with energy-dispersive X-ray spectroscopy (EDX; Oxford Link ISIS) was used to evaluate the surface morphology and elemental composition of the conversion films. The surface composition was also detected by X-ray photoelectron spectroscopy (XPS; VG Scientific ESCA-Lab 250) using 200 W Al Kα radiation. The base pressure is lower than 3 × 10^{-9} mbar. The binding energies were referenced to the C 1s line at 284.8 eV from adventitious carbon. X-ray diffraction (XRD) patterns of samples were recorded with a Rigaku D/MAX-RB diffractometer with monochromatized Cu Kα radiation (λ = 1.5418 Å). Transmission electron microscopy (TEM; JEM-2100M) was used to evaluate the microstructure of the conversion film. The 3D profiles were collected using a digital microscope (KH-7700, HiRox). Fourier transform infrared (FTIR) spectra were collected on a FTIR spectrometer (NEXUS-470, Nicolet Co.) using the KBr method and transmission mode. Raman spectra were collected using a Jobin Yvon (Laboratory RAM HR800) confocal micro-Raman spectrometer. The Ar^+ laser emitting at a wavelength of 488 nm was used as the excitation source. The differential scanning calorimetry (DSC) and thermogravimetric analysis (TGA) curves were obtained using a NETZSCH thermal analysis instruments (STA 449F3). Samples were analyzed in aluminum pans with lids in a dry nitrogen atmosphere. The test temperature was from ambient to 500 °C with a heating rate of 10 °C·min^{-1}. The pH value and conductivity of the phosphoric acid solution were measured using a pH meter (PB-10, Sartorius) and a conductivity meter (DDS-11A, Leici), respectively.

3. RESULTS AND DISCUSSION

3.1. Chemical and Structural Characterizations. Figure 2 shows the images of the surfaces obtained after various deposition durations. As shown in Figure 2a, the bare carbon steel surface is smooth with clear scratches due to mechanical polishing. With a 1-h deposition, a foamlike structure is formed (Figure 2b). The EDX spectrum of the foamlike surface indicates that Fe is the only detected element. It is indicated that no conversion film forms after deposition for 1 h. After deposition for 1.5 h, nanoneedles are obtained (Figure 2c). Also, the EDX spectrum in the inset of Figure 2c shows that O, P, and Fe were detected. It can be deduced that a uniform conversion film forms when the deposition duration is 1.5 h. When the deposition duration increases to 2 h, the nanoneedles grow bigger and form a nanocluster. When the deposition duration is 3 h, the self-assembled nanoclusters grow bigger and form a flower-like structure. Each "flower" consists of nanoneedle petals. The "flower" not only arranges in one flat plane but also grows in the perpendicular direction. New "flower petals" grow on the old ones and form a complex 3D hierarchical micro/nanostructure. As the deposition duration further increases to 4 h, the flower-like clusters grow much bigger. Also, the microstructure has an appearance similar to that of the petal of a chrysanthemum. Thus, continuous flower-like conversion film forms on the carbon steel under an ac voltage after certain deposition durations.

The conversion films obtained in various concentrations of phosphoric acid are also investigated, as illustrated in Figure 3. In the solution containing 0.1 M phosphoric acid, the as-deposited film consists of nanoslices with acuminate shape. The nanoslices distribute randomly with a size of several micrometers (Figure 3a). As the phosphoric acid concentration increases to 0.2 M, it can be seen that the nanoslices grow bigger and thicker, as shown in Figure 3b. After the

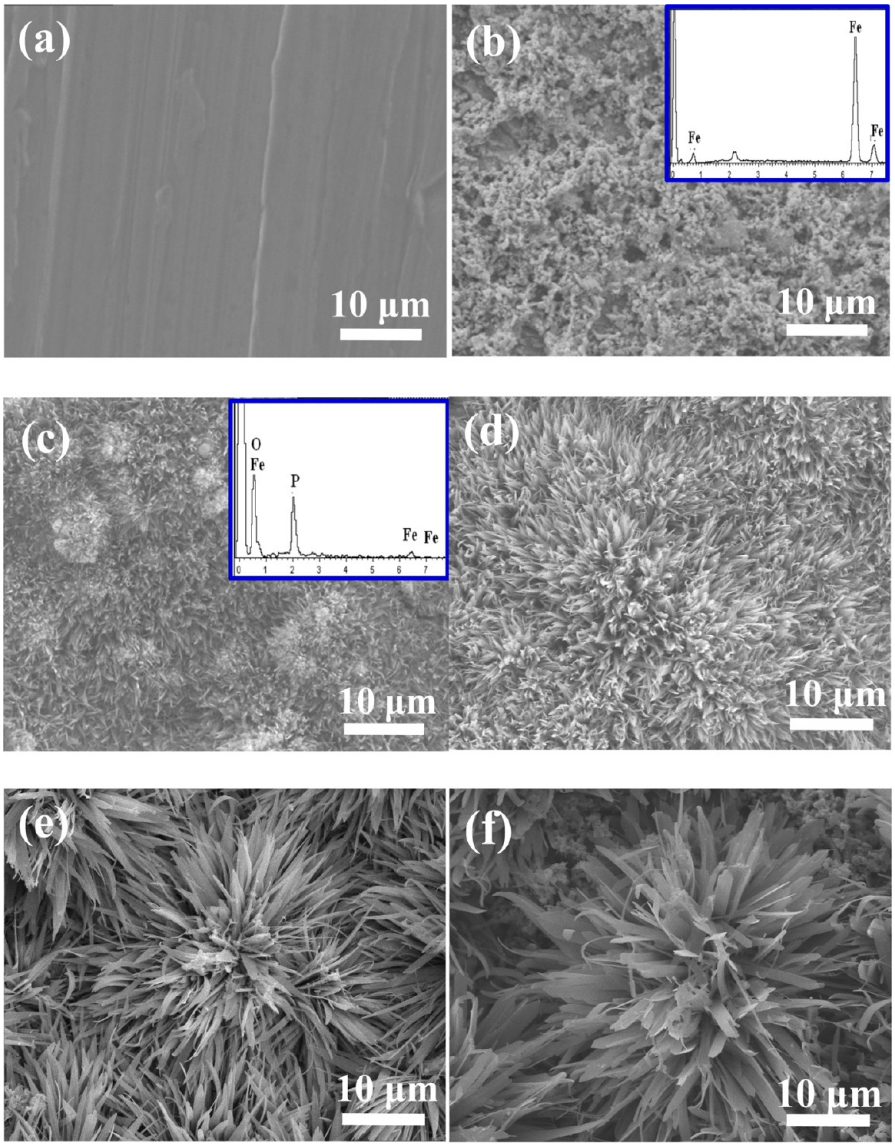

Figure 2. SEM images of the surfaces fabricated in 0.5 M phosphoric acid with various deposition durations: (a) 0 h (bare); (b) 1 h; (c) 1.5 h; (d) 2 h; (e) 3 h; (f) 4 h. The insets are the EDX spectra of the corresponding surfaces.

concentration of phosphoric acid increases up to 0.5 M, as shown in Figure 3c, the morphology of the as-deposited film is much different from that in Figure 3b. As previously observed, the nanoslices grow and concentrate, forming a flower-like structure (see Supporting Information Figure S2b). The diameter of the "flower" is about 10−20 μm, and the petals are 1−2 μm wide and 10 μm long (Figure 3c). When the concentration of phosphoric acid further increases to 1.0 M, the nanoslices grow even bigger, and the size of the "flower" also become larger, as shown in Figure 3d.

The conversion film is amorphous through the characterizations by XRD and high-resolution TEM (HRTEM; see Supporting Information Figure S2a,c). To investigate the structural components of the conversion film, the FTIR and Raman spectra are presented in Figure 4. In the FTIR spectrum (Figure 4a), the broad vibration band at 3440 cm^{-1} is associated with the OH stretching vibration of water molecules and those at 1625 and 1390 cm^{-1} are associated with the bending mode of OH. Vibration bands at 1228 and 1050 cm^{-1} would be the characteristics of P−O and P═O stretching bands in PO_4^{-3}, respectively.[29,30] The absorption band at 580 cm^{-1} is associated with Fe−O bands.[31] Moreover, the Raman spectrum shown in Figure 5b further illustrates the components of the conversion film. The bands at 917, 985, and 1017 cm^{-1} are assigned to the symmetric and asymmetric stretching vibrations of the PO_4^{-3}, respectively.[32,33] The peaks below 600 cm^{-1} are related to different P−O and Fe−O stretching and bending modes.[34,35] Thus, iron phosphate is the main composition of the conversion film.

XPS spectra shown in Figure 5 can further illustrate the surface composition of the conversion film. The XPS survey spectrum indicates that Fe, O, and P can be detected (Figure 5a). Also, C may come from contamination of the samples. Figure 6b shows the high-resolution spectrum of Fe 2p. The binding energies of Fe $2p_{3/2}$ and Fe $2p_{1/2}$ are 711.88 and 725.50 eV, respectively. The distance between Fe $2p_{3/2}$ and Fe $2p_{1/2}$ is 13.62 eV, which presents the typical characteristic of Fe^{3+}.[36] The binding energies of Fe 2p and P 2p (133.55 eV, as shown in Figure 5c) also match the reported results of Yu et al.[37] and Yin et al.,[31] which indicates that the conversion film may be

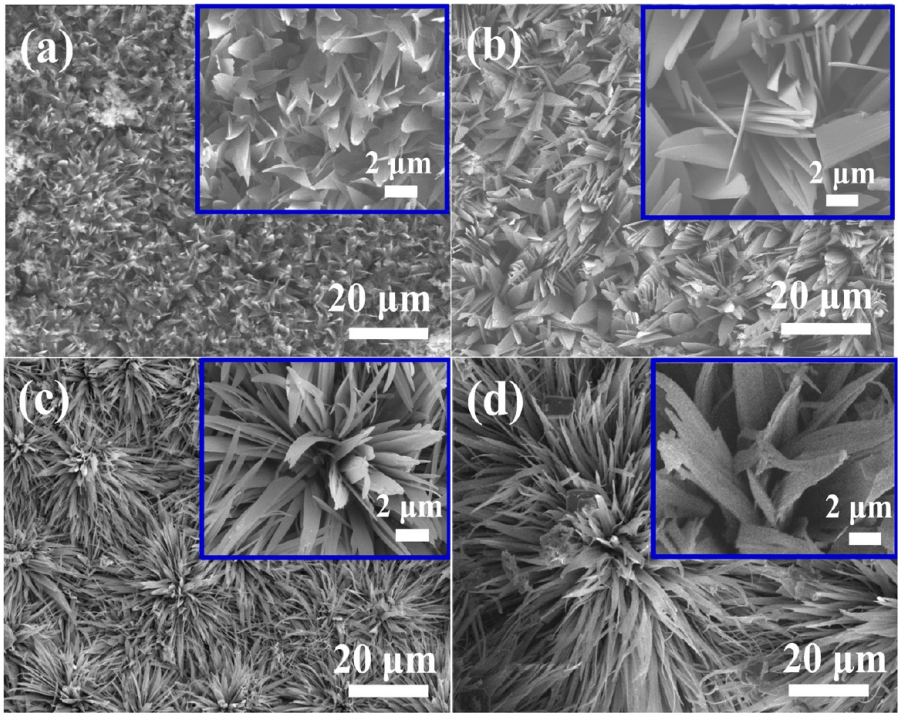

Figure 3. SEM images of the conversion films fabricated in various concentrations of phosphoric acid: (a) 0.1 M; (b) 0.2 M; (c) 0.5 M; (d) 1.0 M. The insets are images of high magnification, and the deposition duration is 3 h.

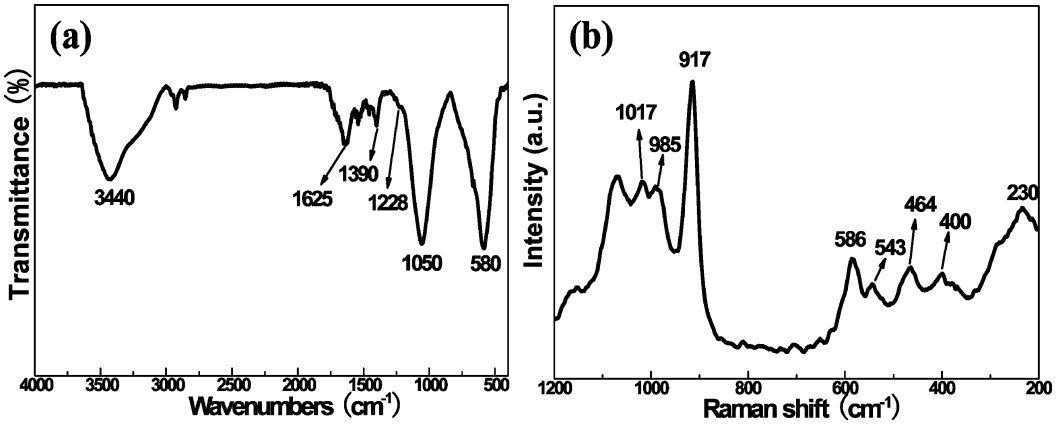

Figure 4. (a) FTIR and (b) Raman spectra of the conversion film.

composed of $FePO_4$. The O 1s spectrum further confirms the composition of the conversion film, as shown in Figure 5d. The O 1s spectrum can be resolved into two components centered at 531.36 and 532.43 eV, corresponding to P═O/Fe−O−P and −OH/H_2O, respectively.[30,38−40] The XPS results indicate that hydrate water exists in the iron phosphate.

To confirm the existence of the hydrate water, thermal analysis curves of the conversion film are obtained, as shown in Figure 6. The DSC curve shows a broad endothermic peak centered at 130 °C. It may be attributed to the dehydration of hydrate metal phosphate.[29,41−43] During the dehydration, the weight of the conversion film sample reduces correspondingly. After the dehydration, the weight percent of the conversion film sample is 82.1% and the weight loss is 17.9%. It is close to the theoretical weight loss of $FePO_4 \cdot 2H_2O$ (18.6%). Thus, the conversion film decomposes according to eq 2:

$$FePO_4 \cdot 2H_2O \xrightarrow{\Delta} FePO_4 + 2H_2O(g) \uparrow \quad \text{(theoretical weight loss: 8.6\%)} \tag{2}$$

Furthermore, the TGA/DSC curves can also indicate that no hydroxyl groups exist in the conversion film. As reported by Rajić et al.,[44] the hydroxyl groups would be removed at 300−400 °C. However, there are no apparent endothermic peaks at 300−400 °C. So, it is reasonable to assume that the conversion film is composed of $FePO_4 \cdot 2H_2O$ according to thermal analysis.

3.2. Deposition Procedure Analysis. To further investigate the ac deposition procedure, the parameters of the phosphoric acid solution were recorded in the ac deposition procedure, as shown in Figure 7. The whole deposition procedure can be divided into four stages. As the carbon steel plates are immersed in the phosphoric acid solution, electrochemical corrosion happens. Fe is oxidized to Fe^{2+} because of the H^+ ionized from phosphoric acid. The reactions will be

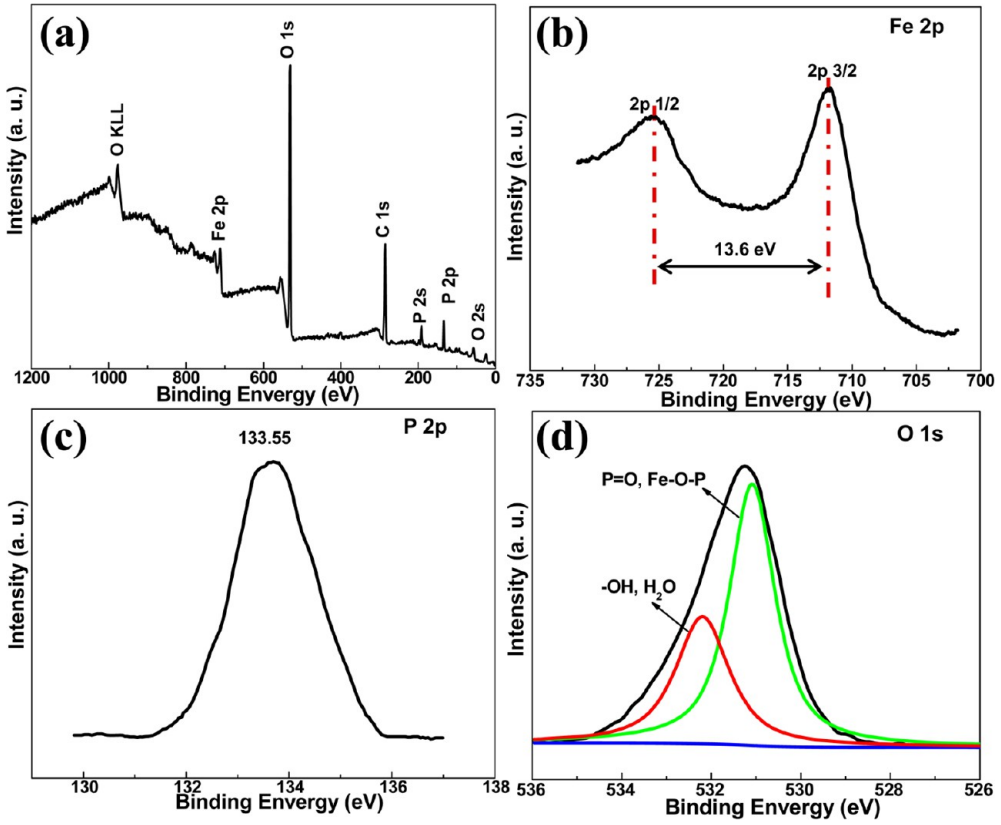

Figure 5. XPS spectra of the conversion film: (a) the survey spectrum and high-resolution spectra of (b) Fe 2p, (c) P 2p, and (d) O 1s.

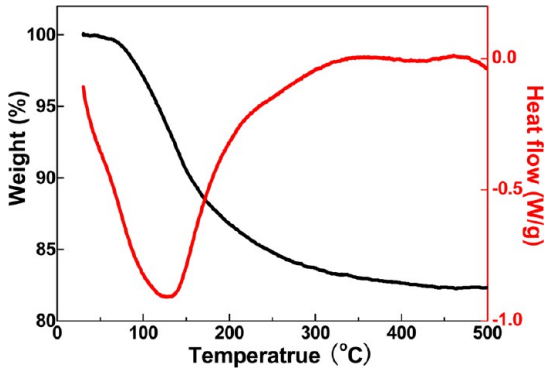

Figure 6. TGA/DSC curves of the conversion film.

greatly accelerated when an ac voltage is applied on the electrodes. Thus, the first stage of the ac deposition is the intense electrolysis of Fe (eq 3). Also, H^+ was reduced to H_2 at this stage (eqs 4 and 5).

$$Fe - 2e^- \leftrightarrow Fe^{2+} \quad (3)$$

$$H_3PO_4 \leftrightarrow H_2PO_4^- + H^+ \quad (4)$$

$$2H^+ + 2e^- \leftrightarrow H_2(g) \quad (5)$$

At the first stage (about 0−25 min), the smooth surface of carbon steel turns into a coarse foamlike structure (Figure 2a,b) because of the electrolysis of Fe and release of H_2 (Figure $7b_1$,b_2). For the consumption of H^+, the pH value and conductivity of the phosphoric acid solution increases and decreases, respectively (Figure $7a_2$). The sharp decrease of the conductivity leads to a great decrease of the current. Also, the increase in temperature is because the electrolysis reaction is an exothermic procedure (Figure $7a_1$). At the second stage (about 25−80 min), the electrolysis reaction rate becomes steady. The electrochemical reaction is the main reaction process at the first and second stages, leading to increases of Fe^{2+} and $H_2PO_4^-$. When the deposition duration is from 80 to 110 min (the third stage), the excessive Fe^{2+} and $H_2PO_4^-$ will react with the dissolved O_2 and $FePO_4{\cdot}2H_2O$ will precipitate, as indicated in eq 6.

$$4Fe^{2+}(l) + 4H_2PO_4^-(l) + O_2(g) + 6H_2O(l) \leftrightarrow 4FePO_4{\cdot}2H_2O(s) + 4H^+(l) \quad (6)$$

The coarse surface of carbon steel provides numerous nucleation sites for the precipitated particles. Thus, a conversion film composed of $FePO_4{\cdot}2H_2O$ grows in situ on the carbon steel surface, as shown in Figure $8b_3$. Because of the continuous decrease of H^+, the electrolysis rate also greatly decreases in the third stage, leading to a sharp decrease of the current. Meanwhile, the change trends of the temperature, pH value, and conductivity become steady (Figure $7a_1$,a_2). At the fourth stage (after 110 min), the conversion film grows gradually and forms a flower-like structure (Figures 2d−f and $7b_4$). There are no apparent changes for the pH value and conductivity of the phosphoric acid solution, which indicates that the electrolysis and precipitation reach equilibrium.

From the above discussion, it is concluded that the whole ac deposition procedure is dominated by both the electrochemical (electrolysis) and chemical (precipitation) reactions. In the first 80 min, the electrochemical reaction is the dominant reaction. The excessive Fe^{2+} and $H_2PO_4^-$ provide conditions for the precipitation. After 80 min, the chemical reaction rate continues

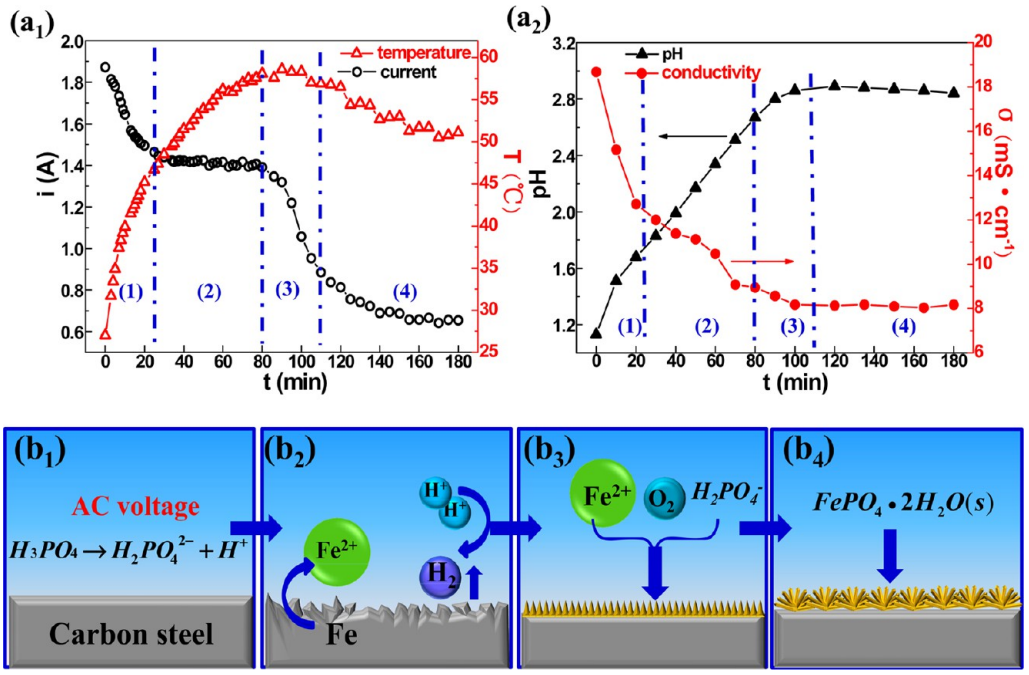

Figure 7. Parameters of the phosphoric acid solution in the ac deposition procedure: (a_1) current and temperature; (a_2) pH value and conductivity. (b_1–b_4) Schematic illustration of the four stages of the deposition procedure.

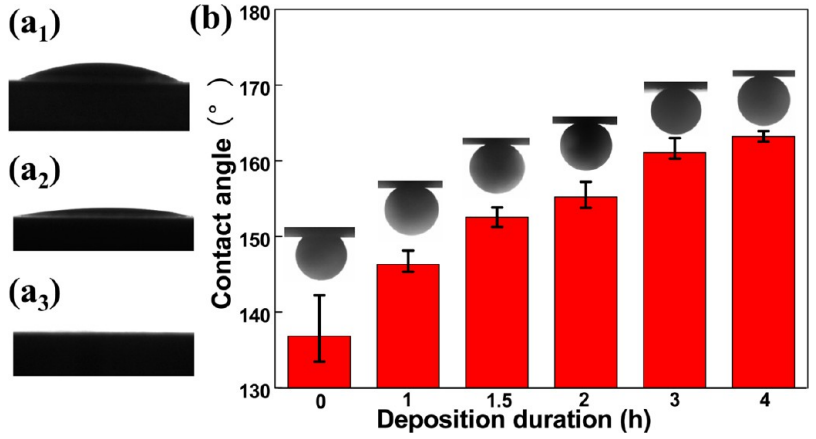

Figure 8. wCAs on samples with various deposition durations: (a_1) 0 h; (a_2) 1 h; (a_3) 1.5 h. (b) Diagram of underwater oCAs on samples obtained with various deposition durations.

to decline, while the precipitation reaction rate continues to rise at the same time. The conversion film will grow steadily when the two reactions reach equilibrium. The detailed analysis on the deposition procedure needs further investigation in later research.

3.3. Wetting Behaviors and Self-Cleaning Performance. The wetting behaviors of the conversion film are shown in Figure 8. The bare carbon steel surface is hydrophilic with a wCA of 25.2 ± 5.0° (Figure 8a_1). However, carbon steel is oleophobic underwater with an oCA of 136.8 ± 4.5° (Figure 8b). The results agree well with the researches of Liu et al.[19] and Jung and Bhushan.[20] When the deposition duration is 1 h, the obtained surface is hydrophilic with a wCA of 7.2 ± 0.8° (Figure 8a_2). When it is immersed into water, the oCA is 146.3 ± 1.4°. When the deposition duration is 1.5 h or longer, the surfaces are superhydrophilic with a wCA of 0°. The water droplet spreads quickly as soon as it contacts with the surfaces, as indicated in Figure 8a_3. Also, these surfaces present underwater superoleophobicity with an oCA larger than 150° (Figure 8b). The oCAs change from 152.5 ± 1.3° to 155.2 ± 1.7° as the deposition duration increases from 1.5 to 2 h. When the deposition duration increases to 3 and 4 h, the oCAs are 161.1 ± 1.4° and 163.2 ± 0.7°, respectively.

The underwater superoleophobicity of the conversion film provides an inspiration for fabricating self-cleaning surfaces to prevent wax deposition in water-contained crude oil. A wax deposition test was applied to evaluate the practical application of the conversion film, and the results are shown in Figure 9. Before the test, the carbon steel surface is silver gray with metallic luster, as illustrated in Figure 9a_1. After the test, a layer of black and brown wax deposits on the surface (Figure 9b). When the deposition duration is 1 h, the DR of the samples is only 5 ± 2%, showing very low wax prevention performance (see Supporting Information video 1). When the deposition duration is 1.5 h, the samples present high self-cleaning performance, which have a DR of 69 ± 12% (Figure 9d). The

dx.doi.org/10.1021/am4030966 | ACS Appl. Mater. Interfaces 2013, 5, 10904–10911

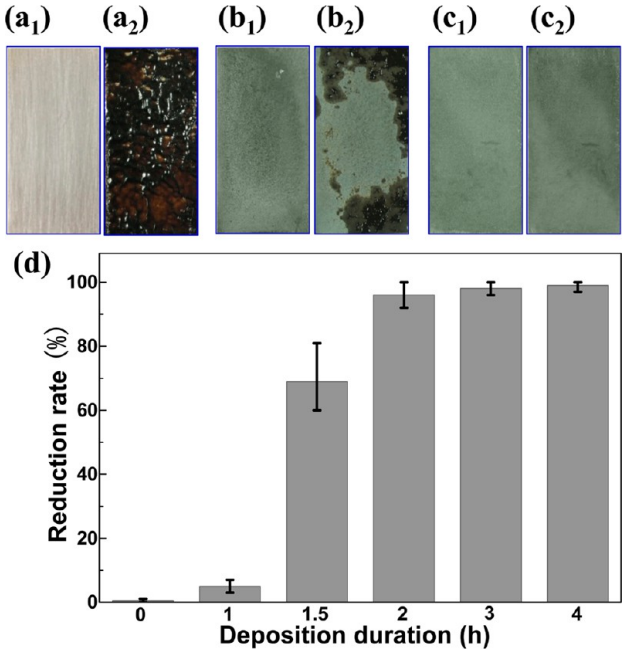

Figure 9. Photographs of samples obtained with various deposition durations: (a_1) 0 h; (b_1) 1.5 h; (c_1) 2 h. (a_2, b_2, and c_2) Same samples after the wax deposition test corresponding to a_1, b_1, and c_1, respectively. (d) Wax DR of samples obtained with various deposition durations.

photographs of the sample before and after the wax deposit test in Figure 9b_1,b_2 also illustrate the self-cleaning performance of the conversion film. The large scatter of DR may be due to the uneven distribution of the conversion film. When the deposition duration increases to 2 h or longer, there are no wax deposits on the surfaces after the test, with DR near 100% (99 ± 1%; Figure 9c_1,c_2,d). Thus, the conversion film presents excellent self-cleaning performance (see Supporting Information video 2). To investigate the durability of the self-cleaning performance for the conversion film, we have implemented the wax deposition test 20 times repeatedly (see Supporting Information Figure S4). After repeating the test 20 times, the conversion film still keeps good self-cleaning performance with DR higher than 95%. The good durability of the self-cleaning performance makes it possible to use such a conversion film in practical applications.

The mechanisms of underwater superoleophobicity and self-cleaning performance are also discussed, as illustrated in Figure 10. It is known that the wettability of a surface depends on the surface composition and microstructure. The wetting states in a water−oil−solid system could also be divided into Young's state, Wenzel's state, Wenzel−Cassie's transitional state, and Cassie's state.[45] In the water−oil-solid system, the underwater oCA can be expressed[19,20] by

$$\cos\theta_{OW} = \frac{\gamma_{OA}\cos\theta_O - \gamma_{WA}\cos\theta_W}{\gamma_{OW}} \quad (7)$$

where γ_{OA}, γ_{WA}, and γ_{OW} are the surface tensions of oil−air, water−air, and oil−water interfaces, respectively. Also, θ_{OW}, θ_O, and θ_W are the CAs of oil in water, oil in air, and water in air, respectively.

As indicated in eq 7, an oleophobic state can be created when $\gamma_{OA}\cos\theta_O < \gamma_{WA}\cos\theta_W$. Because the oil surface tension is much lower than that of water ($\gamma_{OA} < \gamma_{WA}$), most hydrophilic

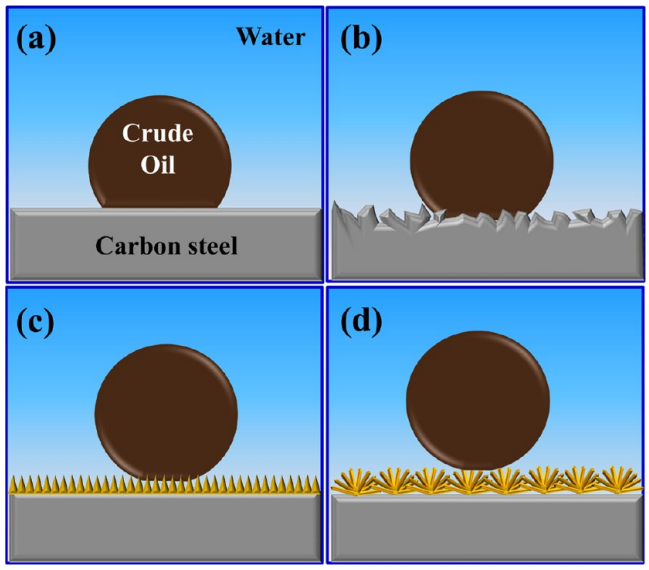

Figure 10. Schematic of the wetting states in the oil−water−solid system: (a) Young's state; (b) Wenzel's state; (c) Wenzel−Cassie's transitional state; (d) Cassie's state.

surfaces ($\cos\theta_W > 0$) can be underwater oleophobic in the water−oil−solid system. The smooth carbon steel is hydrophilic in air, and it turns to oleophobic in water. It is the underwater Young's state, as shown in Figure 10a. With an increase of the deposition duration, the surface morphology becomes rougher and rougher (see Supporting Information Figure S3). When the surfaces are immersed to water, different wetting states form. The rough structure can improve the hydrophilicity of the surface in air, according to Wenzel's theory.[46] When the deposition duration is 1 h, the oleophobicity is promoted because the electrolytic coarse surface and the underwater Wenzel's state form (Figure 10b). The oCAs are very large on this surface (Figure 8b); however, the SAs of crude oil are also large, presenting high oil adhesion (see Supporting Information Figure S5). So, wax is prone to deposit on these surfaces. After deposition for 1.5 h, a superhydrophilic conversion film with nanoneedle structure further increases the underwater oCAs. Water can be trapped in the micro/nanostructure (Figure 10c), forming the underwater Wenzel−Cassie's transitional state. The surface is superoleophobic and has lower SAs than that without a conversion film. So, this surface presents a relatively high self-cleaning performance (Figure 9b_2,d). When the deposition duration further increases to 2 h or longer, the conversion film has a hierarchical micro/nanostructure, which could trap much more water. The trapped water would dramatically reduce the contact area between the crude oil and conversion film. In that case, an underwater Cassie's state forms (Figure 10d), leading to superoleophobicity and low oil adhesion (see Supporting Information video 3). Thus, the precipitated wax can hardly adhere on the conversion film. Consequently, the conversion film presents high self-cleaning performance in the water-contained crude oil with no wax deposition.

4. CONCLUSION

Inspired by the fish scale and clam's shell, we have designed and fabricated conversion films using a novel in situ ac deposition method. Under the ac voltage for several hours, amorphous iron phosphate precipitates and grows in situ on the carbon

steel from the phosphoric acid solution, forming a flower-like conversion film. The deposition procedure is discussed, and it can be divided into four stages: intense electrolysis, steady electrolysis, precipitation, and steady growth. The conversion film is superhydrophilic in air and superoleophobic underwater. After the wax deposition test, almost no wax deposits on the conversion film and the DR are near 100% (when the deposition duration is longer than 2 h). Thus, the conversion film presents excellent self-cleaning performance in the water-contained crude oil. Moreover, the self-cleaning performance has a good durability. The self-cleaning performance is attributed to the superhydrophilic component (iron phosphate) and hierarchical micro/nanostructure of the conversion film. This study provides a time-saving and low-cost strategy to construct self-cleaning films that could be potentially applied to crude oil pipelines or oil-polluted water.

■ ASSOCIATED CONTENT

Ⓢ Supporting Information

Schematic figure of ac deposition, characteristics of the crude oil, XRD patterns and TEM and HRTEM images of conversion films, 3D roughness profile of the surfaces with various ac deposition durations, result of the wax deposition durability test, and wetting behaviors of a crude oil droplet on the surface in the water environment. This material is available free of charge via the Internet at http://pubs.acs.org.

■ AUTHOR INFORMATION

Corresponding Author

*E-mail: liuhc@buaa.edu.cn. Tel: +86 1082317113. Fax: +86 1082317133.

Notes

The authors declare no competing financial interest.

■ ACKNOWLEDGMENTS

The authors are very grateful for support from the National Natural Science Foundation of China (Grant 51071012).

■ REFERENCES

(1) Thanh, N. X.; Hsieh, M.; Philp, R. P. *Org. Geochem.* **1999**, *30*, 119−132.
(2) Dirand, M.; Chevallier, V.; Provost, E.; Bouroukba, M.; Petitjean, D. *Fuel* **1998**, *77*, 1253−1260.
(3) Lazar, I.; Voicu, A.; Nicolescu, C.; Mucenica, D.; Dobrota, S.; Petrisor, I. G.; Stefanescu, M.; Sandulescu, L. *J. Pet. Sci. Eng.* **1999**, *22*, 161−169.
(4) Chen, W.; Zhao, Z.; Yin, C. *Fuel* **2010**, *89*, 1127−1132.
(5) Tung, N. P.; Vinh, N. Q.; Phong, N. T. P.; Long, B. Q. K.; Hung, P. V. *Phys. Rev. B: Condens. Matter* **2003**, *327*, 443−447.
(6) Quintella, C. M.; Musse, A. P. S.; Castro, M. T. P. O.; Scaiano, J. C.; Mikelsons, L.; Watanabe, Y. N. *Energy Fuels* **2006**, *20*, 620−624.
(7) Blossey, R. *Nature* **2003**, *2*, 301−306.
(8) Furstner, R.; Barthlott, W.; Neinhuis, C.; Walzel, P. *Langmuir* **2005**, *21*, 956−961.
(9) Wong, T.; Kang, S. H.; Tang, S. K. Y.; Smythe, E. J.; Hatton, B. D.; Grinthal, A.; Aizenberg, J. *Nature* **2011**, *477*, 443−447.
(10) Dufour, R.; Brunet, P.; Harnois, M.; Boukherroub, R.; Thomy, V.; Senez, V. *Small* **2012**, *8*, 1229−1236.
(11) Liu, H.; Szunerits, S.; Pisarek, M.; Xu, W.; Boukherroub, R. *ACS Appl. Mater. Interfaces* **2009**, *1*, 2086−2091.
(12) Coffinier, Y.; Galopin, E.; Szunerits, S.; Boukherroub, R. *J. Mater. Chem.* **2010**, *20*, 10671−10675.
(13) Dufour, R.; Harnois, M.; Thomy, V.; Boukherroub, R.; Senez, V. *Soft Matter* **2011**, *7*, 9380−9387.
(14) Perry, G.; Coffinier, Y.; Thomy, V.; Boukherroub, R. *Langmiur* **2012**, *28*, 389−395.
(15) Cassie, A. B. D.; Baxter, S. *Trans. Faraday Soc.* **1944**, *40*, 546−551.
(16) Dos Santos, R. G.; Mohamed, R. S.; Bannwart, A. C.; Loh, W. *J. Pet. Sci. Eng.* **2006**, *51*, 9−16.
(17) Starkweather, B. A.; Zhang, X. S.; Counce, R. M. *Ind. Eng. Chem. Res.* **2000**, *39*, 362−366.
(18) Jarn, M.; Granqvist, B.; Lindfors, J.; Kallio, T.; Rosenholm, J. B. *Adv. Colloid Interfaces* **2006**, *123−126*, 137−149.
(19) Liu, M.; Wang, S.; Wei, Z.; Song, Y.; Jiang, L. *Adv. Mater.* **2009**, *21*, 665−669.
(20) Jung, Y. C.; Bhushan, B. *Langmuir* **2009**, *25*, 14165−14173.
(21) Hejazi, V.; Nosonovsky, M. *Langmuir* **2011**, *28*, 2173−2180.
(22) Hejazi, V.; Nyong, A. E.; Rohatgi, P. K.; Nosonovsky, M. *Adv. Mater.* **2012**, *24*, 5963−5966.
(23) Xue, Z.; Wang, S.; Lin, L.; Chen, L.; Liu, M.; Feng, L.; Jiang, L. *Adv. Mater.* **2011**, *23*, 4270−4273.
(24) Wen, Q.; Di, J.; Jiang, L.; Yu, J.; Xu, R. *Chem. Sci.* **2013**, *4*, 591−595.
(25) Liu, X.; Zhou, J.; Xue, Z.; Gao, J.; Meng, J.; Wang, S.; Jiang, L. *Adv. Mater.* **2012**, *24*, 3401−3405.
(26) Liu, X.; Gao, J.; Xue, Z.; Chen, L.; Lin, L.; Jiang, L.; Wang, S. *ACS Nano* **2012**, *6*, 5614−5620.
(27) Ball, P. *Nature* **1999**, *400*, 507−509.
(28) Dos Santos, J. D. S. T.; Fernandes, A. C.; Giulietti, M. *J. Pet. Sci. Eng.* **2004**, *45*, 47−60.
(29) Scaccia, S.; Carewska, M.; Bartolomeo, A. D.; Prosini, P. P. *Thermochim. Acta* **2002**, *383*, 145−152.
(30) Daou, T. J.; Begin-Colin, S.; Grenèche, J. M.; Thomas, F.; Derory, A.; Bernhardt, P.; Legaré, P.; Pourroy, G. *Chem. Mater.* **2007**, *19*, 4494−4505.
(31) Yin, Y.; Hu, Y.; Wu, P.; Zhang, H.; Cai, C. *Chem. Commun.* **2012**, *48*, 2137−2139.
(32) Frost, R. L.; Weier, M. L.; Erickson, K. L.; Carmody, O.; Mills, S. J. *J. Raman Spectrosc.* **2004**, *35*, 1047−1055.
(33) Fang, X.; Ray, C. S.; Moguš-Milanković, A.; Day, D. E. *J. Non-Cryst. Solids* **2001**, *283*, 162−172.
(34) Pasternak, M. P.; Rozenberg, G. K.; Milner, A. P.; Amanowicz, M.; Zhou, T.; Schwarz, U.; Syassen, K.; Dean Taylor, R.; Hanfland, M.; Brister, K. *Phys. Rev. Lett.* **1997**, *79*, 4409−4412.
(35) Zhang, L.; Brow, R. K. *J. Am. Ceram. Soc.* **2011**, *94*, 3123−3130.
(36) Wanger, C. D. *Handbook of X Ray Photoelectron Spectroscopy*; Riggs, W. M., Davis, L. E., Moulder, J. F., Muilenberg, G. E., Eds.; Perkin-Elmer Corp.: Waltham, MA, 1979; Vol. *2*, p 76.
(37) Yu, D.; Wu, C.; Kong, Y.; Xue, N.; Guo, X.; Ding, W. *J. Phys. Chem. C* **2007**, *111*, 14394−14399.
(38) Morgan, W. E.; Van Wazer, J. R.; Stec, W. J. *J. Am. Chem. Soc.* **1973**, *95*, 751−755.
(39) Tosatti, S.; Michel, R.; Textor, M.; Spencer, N. D. *Langmuir* **2002**, *18*, 3537−3548.
(40) Adden, N.; Gamble, L. J.; Castner, D. G.; Hoffmann, A.; Gross, G.; Menzel, H. *Langmuir* **2006**, *22*, 8197−8204.
(41) Galwey, A. K. *Thermochim. Acta* **2000**, *355*, 181−238.
(42) Scaccia, S.; Carewska, M.; Bartolomeo, A. D.; Prosini, P. P. *Thermochim. Acta* **2003**, *397*, 135−141.
(43) Scaccia, S.; Carewska, M.; Prosini, P. P. *Thermochim. Acta* **2004**, *413*, 81−86.
(44) Rajić, N.; Gabrovšek, R.; Kaučič, V. *Thermochim. Acta* **2000**, *359*, 119−122.
(45) Huang, Y.; Liu, M.; Wang, J.; Zhou, J.; Wang, L.; Song, Y.; Jiang, L. *Adv. Funct. Mater.* **2011**, *21*, 4436−4441.
(46) Wenzel, R. N. *Ind. Eng. Chem.* **1936**, *28*, 988−994.